ELSEVIER

Contents lists available at ScienceDirect

# Biosensors and Bioelectronics

journal homepage: www.elsevier.com/locate/bios





# Waterproof, flexible field-effect transistors with submicron monocrystalline Si nanomembrane derived encapsulation for continuous pH sensing

Shulin Chen<sup>a</sup>, Yan Dong<sup>a</sup>, Tzu-Li Liu<sup>a</sup>, Jinghua Li<sup>a,b,\*</sup>

- <sup>a</sup> Department of Materials Science and Engineering, The Ohio State University, Columbus, OH, 43210, USA
- <sup>b</sup> Chronic Brain Injury Program, The Ohio State University, Columbus, OH, 43210, USA

#### ARTICLE INFO

Keywords: Field-effect transistors Biochemical sensing Potentiometry Flexible electronics pH sensors

#### ABSTRACT

To understand the physio-pathological state of patients suffering from chronic diseases, scientists and clinicians need sensors to track chemical signals in real-time. However, the lack of stable, safe, and scalable biochemical sensing platforms capable of continuous operation in liquid environments imposes significant challenges in the timely diagnosis, intervention, and treatment of chronic conditions. This work reports a novel strategy for fabricating waterproof and flexible biochemical sensors with active electronic components, which feature a submicron encapsulation layer derived from monocrystalline Si nanomembranes with a high structural integrity due to the high formation temperature (>1000 °C). The ultrathin, yet dense and low-defect encapsulation enables continuous operation of field-effect transistors in biofluids for chemical sensing. The excellent stability in liquid environment and pH sensing performance of such transistors suggest their great potential as the foundation of waterproof and scalable biochemical sensors with active functionalities in the future. The understandings, knowledge base, and demonstrations for pH sensing reported here set the stage for the next generation long-term biosensing with a broad applicability in biomedical research, food science, and advanced healthcare.

# 1. Introduction

Biofluids in human bodies contain a variety of chemical biomarkers that could reveal health and age-based conditions crucial to biomedical research and clinical medicine (Andreu-Perez et al., 2015; Arakawa et al., 2016; Gao et al., 2016; Kim et al., 2018a; Lee et al., 2018; Martín et al., 2017). In recent years, interests in label-free, sensitive, and selective detection of biochemical signals in biofluids (e.g., blood (Agoston et al., 2017; Ausländer et al., 2014; Lucisano et al., 2017), cerebrospinal fluid (Arvand and Ghodsi, 2014; Wang et al., 2015), sweat (Gao et al., 2016; Koh et al., 2016; Rose et al., 2015), saliva (Arakawa et al., 2016; Malon et al., 2014), and tears (Iguchi et al., 2007; Kim et al., 2017)) have motivated continued research efforts in developing novel sensing strategies and tools towards real-time, accurate, personalized, and continuous health monitoring outside of laboratory and hospital settings. In particular, the continuous monitoring of important diagnostic/prognostic biomarkers using wearable and implantable biosensors can provide valuable evidence about disease progression. As an example, the chronic kidney disease (CKD) involves lasting and progressive damages over time that can eventually result in kidney failure (Levey and Coresh, 2012). To this end, bio-integrated sensors can collect timely information about the health status of patients with CKD, such as pH value of (Pavuluri et al., 2019) and urea concentration in sweat (Huang et al., 2002; Keller et al., 2016; Zhang et al., 2019), and creatinine concentration in serum (Pandya et al., 2016; Renda, 2017). The advent of continuous monitoring can create opportunities for data science and artificial intelligence to understand the pathway and impact of diseases at large scales.

Among various emerging tools, sensors based on field-effect transistors (FETs) have attracted considerable attentions due to the signal amplification capability, high sensitivity, fast response time, potential for miniaturization and multiplexing, and compatibility with scaled manufacturing processes such as complementary metal-oxide-semiconductor (CMOS) technologies (Chen et al., 2011; Janata, 1994; Kaisti, 2017; Lanuzza et al., 2015; Lee et al., 2009; Mao et al., 2017; Mu et al., 2014; Nguyen et al., 1992). In particular, electronics with arrayed pixel units derived from silicon substrates provide a realistic way for scaled integration of sensors with on-chip signal processing and multiplexing capabilities (Wu et al., 2021). The use of sensor arrays in biosensing allows for real-time imaging of biomarker concentration and

<sup>\*</sup> Corresponding author. Department of Materials Science and Engineering, The Ohio State University, Columbus, OH, 43210, USA. *E-mail address:* li.11017@osu.edu (J. Li).

flow with a high spatiotemperoal resolution (Asher et al., 2002). Despite the success in the development of FET chemical sensors with different semiconductor materials, device structures, and various functionalization layers, a common and critical challenge is the stability of sensors in liquid environments. Thin films (e.g., metals, ceramics, polymers) deposited at relatively low temperatures usually have a limited encapsulation capability due a combination of extrinsic (e.g., grain boundaries, pin-hole defects) and intrinsic properties (e.g., free volume) (Fang et al., 2016). As a result, water and ions in the target fluids can diffuse to the active regions, resulting in signal drifts or even catastrophic failures within a short time (Bae et al., 2013; Fang et al., 2016; Kim et al., 2018b). However, continuous monitoring of blood pH during surgery requires an accuracy over a period of up to ~10 h (Elyasi et al., 2018). The issue is even more critical when it involves long-term biochemical sensing applications.

Based on pioneering studies (Fang et al., 2016), this work reports a materials strategy for building a class of waterproof and flexible biochemical sensors to address this issue. This strategy exploits a submicron thin-film biofluid barrier structure with islands of conductive Si nanomembranes (NMs) embedded in thermally grown SiO<sub>2</sub> (t-SiO<sub>2</sub>) with intimate, chemically bonded interface formed during thermal oxidation at a temperature of above 1000 °C. A layer of metal oxide (e. g., Al<sub>2</sub>O<sub>3</sub>) serves as the sensing interface for the detection of protons in solution. In this design, the coupling between the sensing layer in contact with biofluids and encapsulated transistors enables the chemical-to-electrical signal transduction. The system converts a surface potential change caused by chemical adsorption into a modification in the charge transport behavior in the semiconductor channels. Characterizations of electrical properties, signal drift behavior, and pH sensing performance examine fundamental properties of this flexible potentiometric sensing platform. The device concept, materials design, and integration strategy presented here provide a realistic pathway towards a variety of flexible, waterproof, and bio-integrated chemical sensors having on-chip signal amplification and multiplexing capabilities for detecting diagnostic/prognostic biomarkers, with broad applicability in next-generation advanced healthcare and other areas.

# 2. Materials, device fabrication, and methods

This section provides experimental details about materials, design, and fabrication procedures for the waterproof FETs and the characterization of their electrical performances in pH sensing.

#### 2.1. Devices fabrication

A step-by-step schematic illustration of fabrication procedures of the waterproof transistors appears in Fig. S1. The fabrication of device started with a silicon-on-insulator (SOI) substrate (Soitec). The wafer consisted of a top layer of lightly doped p-type Si (crystal orientation: (100)) with a doping concentration of  $10^{15}$  cm<sup>-3</sup> (resistivity: 8.5–11.5  $\Omega$ cm<sup>-1</sup>). Thermal oxidation of the device-grade Si on top formed a layer of SiO<sub>2</sub> (~200 nm) as the diffusion mask. Photolithographic patterning followed by reactive ion etching (RIE) with CF<sub>4</sub>/O<sub>2</sub> and buffered oxide etching (BOE) yielded opening on the diffusion mask, followed by thermal diffusion of boron (1000  $^{\circ}$ C) to form p<sup>++</sup>-Si in the exposed areas (concentration:  $\sim 10^{20}$  cm<sup>-3</sup>). Washing with hydrofluoric acid removed SiO<sub>2</sub>. Plasma enhanced chemical vapor deposition (PECVD) yielded another layer of SiO<sub>2</sub> (~400 nm) as a second diffusion mask. Patterning, etching, and doping with phosphorus via thermal diffusion (1000 °C) or spin-on doping (P509; Filmtronics, Inc.) (900  $^{\circ}$ C) formed n<sup>++</sup>-Si (concentration:  $\sim 10^{19} \, \text{cm}^{-3}$ ) as the backplane for n-type MOSFETs, followed by the removal of the second diffusion mask using hydrofluoric acid. Photolithographic patterning and etching out extra Si by RIE with SF<sub>6</sub> yielded Si islands on t-SiO2. Thermal oxidation at 1000 °C in a tube furnace followed by atomic layer deposition (ALD, Picosun SUNALE R-150B) at 80 °C produced a gate dielectric stack of SiO<sub>2</sub> (~63 nm) and

Al<sub>2</sub>O<sub>3</sub> (~13 nm). Patterning, etching and metallization (10 nm Cr/200 nm Au) using electron-beam evaporation finished the fabrication of the transistor. A coating layer of polyimide (PI 2545; HD Microsystems)  $(\sim 2 \,\mu\text{m})$  on the top side of the device encapsulated the transistor. A layer of Al<sub>2</sub>O<sub>3</sub> deposited by ALD on PI served as an adhesion promoter for subsequent bonding process. A separate step prepared a sheet of Al<sub>2</sub>O<sub>3</sub> (~20 nm) coated Kapton film (~13  $\mu m)$  laminated on a glass slide with polydimethylsiloxane (PDMS). A mechanical bonding process joined the PI side of the device and the Kapton film using a silicone adhesive (Kwik-Sil; World Precision Instruments). The removal of the backside Si handle wafer using inductive coupled plasma (ICP) RIE with SF<sub>6</sub>/O<sub>2</sub> exposed the bottom surface of t-SiO<sub>2</sub> on SOI followed by forming small openings by RIE and BOE in SiO<sub>2</sub> aligned to p<sup>++</sup>-Si and terminal contact pads. ALD formed 20 nm Al<sub>2</sub>O<sub>3</sub> at 150 °C on top of p<sup>++</sup>-Si as sensing layer. In the end, etching out Al<sub>2</sub>O<sub>3</sub> on the contact pads with BOE completed the fabrication process.

#### 2.2. Thin-film dissolution rate test

The study used phosphate buffered saline (PBS) solution (pH = 7.4) in plastic bottles at 37  $^{\circ}C$  to provide environment for the dissolution test of  $p^{++}\text{-Si}$ , t-SiO $_2$  and ALD-Al $_2\text{O}_3$ . During each test, rinsing the samples followed by measuring the thickness of the thin films using reflectometry (Nanospec 3000 PH Thin Film Reflectometer) periodically determined the dissolution rates of the NMs.

#### 2.3. Electrical performance characterization

A four-point probe (Jandel MHP/RM3) measured the sheet resistance of the Si NMs after doping. The electrical characterization system for transistors consisted of a probe station and a semiconductor parameter analyzer (Keysight B1500A). A Ag/AgCl or a Pt wire served as the reference electrode. An EasyEXPERT software provided the user interface for measurement setup and execution to recording and analysis.  $V_{DS}$  used for the study was 100 mV.

# 2.4. Stability test

The stability study of the device included two test modes: (1) for the ion-sensitive FET (ISFET) mode, a reference electrode electrically biased the PBS solution for gating through the ultrathin encapsulation layer which protected the underlying electronics. The source and drain electrodes connected to the probe station through the terminal pads located away from the solution; and (2) for the metal-oxide-semiconductor FET (MOSFET) mode, the source, drain and gate electrodes all connected to the probe station through the metal pads while the active part of the device was exposed to PBS solution. In both test modes,  $V_{DS}$  and  $V_{GS}$  were continuously applied to the transistors throughout the time course of the study. For acceleration tests, a hot plate controlled the temperature of the system at 75, 80, 85, 90, and 100 °C, and an electrochemical station measured the leakage current across the t-SiO<sub>2</sub> layer.

#### 2.5. Enzymatic catalysis study

The enzyme solutions were prepared by dissolving lyophilized urease and penicillinase in PBS solution, respectively. Injecting enzyme solutions to the corresponding substrate solutions triggered the enzymatic catalysis. A sensor recorded changes in pH value as a function of time. Conversion of the change in  $I_{DS}$  into a shift in the threshold voltage ( $V_{th}$ ) quantified the modulation in surface potential. A commercial pH meter (FiveEasy Benchtop F20 pH/mV Standard Kit) provided comparison for the sensing results. For the evaluation of H<sup>+</sup> concentration change, the initial pH values of solutions were determined by calibrating the systems using standard buffer solutions as references before the test.

#### 2.6. Detection of sweat pH during exercise

Informed written consent was obtained prior to the research. The study was performed in compliance with a protocol approved by the Institutional Review Board at The Ohio State University (study number: 2020H0293).

#### 3. Results and discussion

This section provides results of systematic studies on the materials and devices, including design principles, mechanical robustness, stability and drift behavior in liquid environment, and performances in pH sensing.

# 3.1. Design of MOSFET chemical sensors with monocrystalline Si-Derived encapsulation

The fabrication begins with a SOI substrate having a top layer of device-grade monocrystalline Si and a buried t-SiO<sub>2</sub> layer (thickness: <  $1~\mu m$ ). Doping, photolithographic patterning, and etching steps form isolated NMs of  $n^{++}$ -Si (concentration:  $\sim 10^{19}~\text{cm}^{-3}$ , sheet resistance: ~270  $\Omega$  sq<sup>-1</sup>) and p<sup>++</sup>-Si (concentration: ~10<sup>20</sup> cm<sup>-3</sup>, sheet resistance:  $\sim$ 50  $\Omega$  sq<sup>-1</sup>) on the t-SiO<sub>2</sub> layer (Fig. 1A). Subsequent oxidation, deposition, etching, and metallization steps create n-type MOSFETs on the SOI substrate, with gate electrodes electrically connected to the patterned p++-Si regions (Fig. 1B). Spin-coating of a uniform layer of polyimide (PI) on the top side of the substrate encapsulates the electronic system. Bonding the top layer of the device to a temporary handling substrate using a commercial adhesive followed by removing the backside Si handle wafer exposes the bottom surface of t-SiO<sub>2</sub> as a barrier against biofluids (Fig. 1C and S2). Flipping the device and etching out small openings in SiO<sub>2</sub> aligned to p<sup>++</sup>-Si and terminal contact pads establish conductive pathways to the sensing layers and the electrical characterization system (Fig. 1D). ALD forms an ultrathin layer of Al<sub>2</sub>O<sub>3</sub> covering p<sup>++</sup>-Si for sensing (Fig. 1E). Finally, peeling off the device from the glass substrate completes the fabrication process and yields a flexible chemical sensor with a submicron, waterproof encapsulation layer covering the entire active region of the device (Fig. 1F). Currently, the cost of such devices is relatively higher compared to that of conventional FETs, as the fabrication involves additional backbonding and back-etching processes to transfer the encapsulation layers from rigid SOI to flexible substrates. However, reducing the cost is possible by further optimizing the processing control, improving the yield, and scaling manufacturing using CMOS technologies. Compared to other FETs, one advantage of the devices is that the encapsulation layers derived from monocrystalline Si possess a very low defect density due to the high formation temperature (>1000 °C) and the high structural integrity of the growth template. Therefore, such devices can have

a longer lifetime in liquid environment compared to conventional FETs (Fang et al., 2016), which provides a realistic pathway for continuous monitoring of biochemical processes using active electronics. It should be noted that based on the cleanroom environments and equipment available, the yield of working devices is  $\sim$ 30%, which is lower than that of conventional FETs. Key factors leading to failures in fabrication and possible solutions are discussed as follows: (1) the SOI wafer used for fabrication is thinner ( $\sim$ 100–200 µm) than normal ( $\sim$ 500 µm) in order to minimize the time needed for back-etching. This could lead to unexpected cracking of devices during the fabrication steps. Identifying a suitable balance between the back-etching time and robustness of SOI for handling could potentially address this issue; (2) opening windows on t-SiO<sub>2</sub> using BOE may result in the cracking of the encapsulation layer due to the penetration of etchant through the unprotected edges of the system and defects on t-SiO2 propagated during the fabrication steps. This problem can be improved by decreasing the time used for wet etching, as well as optimizing the processing control during device fabrication.

Fig. 2A shows the side-view schematic illustration of an encapsulated electronic device. An exploded view highlighting key functional layers of the device appears in Fig. S3. An applied gate voltage modulates the charge carrier density in the semiconductor channel and thereby controls its conductance either through the top gate electrode ( $V_{TG}$ ) using a probe tip or through the liquid gate ( $V_{LG}$ ) using a reference electrode. For pH sensing in solution, reversible protonation and deprotonation occur and modify the surface potential. The following equation describes the gate to source bias ( $V_{GS}$ ) of a FET sensor with a liquid gate (Garcia-Cordero et al., 2018):

$$V_{GS} = V_{ref} - \psi_0 + \chi^{sol} - \frac{\varphi_{Si}}{q} - \frac{Q_t}{C_{ox}} + 2\varphi_F$$
 (1)

where  $V_{ref}$  is the voltage applied to the reference electrode,  $\psi_0$  is the surface potential at the solution-sensor interface,  $\chi^{sol}$  is the surface dipole potential of the solvent,  $\varphi_{Si}$  is the work function of the Si channel, q is the elementary charge,  $Q_t$  is the sum of depletion layer charges in the semiconductor channel, accumulated charges in the dielectric layers, and the interface trap charges,  $C_{ox}$  is the capacitance of dielectrics, and  $2\varphi_F$  is the surface potential at the channel and dielectrics interface in strong inversion.

As illustrated in the equivalent circuit in Fig. 2B, the system contains capacitors in series connection between the source and liquid gate electrodes, which are the depletion region in the semiconductor channel  $(C_{ch})$ , the top gate dielectrics  $(C_{TG})$ , the metal oxide pH sensing layer  $(C_{Sens})$ , and the electric double layer  $(C_{Stern})$  and  $(C_{Goty})$ . Fig. 2C (left, middle) shows representative photographs of such waterproof sensors, with a total thickness of  $\sim$ 20 µm. Optical images of the n-type MOSFET and the p<sup>++</sup>-Si gate electrode with via opening on SiO<sub>2</sub> appear in Fig. 2C (right). The effective channel length is  $\sim$ 19.2 µm (Supplementary Note

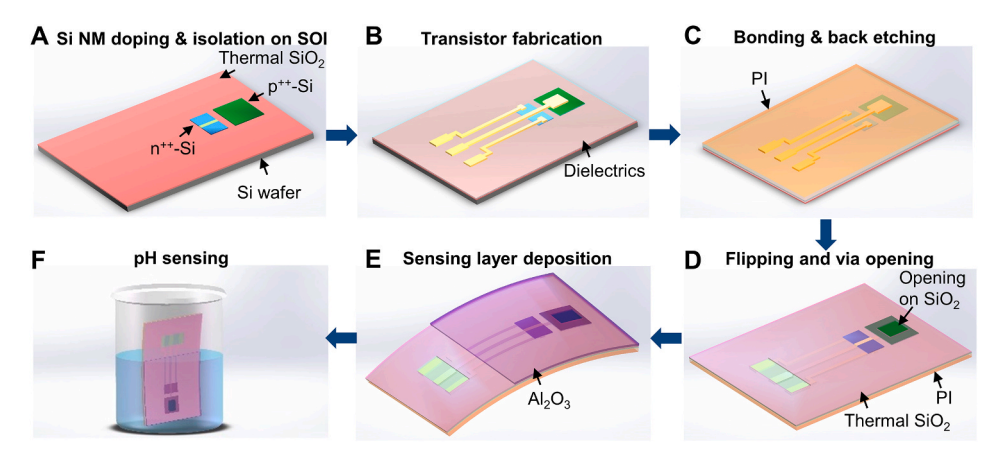


Fig. 1. Materials, design, and fabrication procedure for waterproof FET sensors with monolithically bonded  $SiO_2$  and Si as biofluid barriers for pH sensing. (A) Doping and patterning  $n^{++}$ -Si and  $p^{++}$ -Si NMs on a SOI substrate; (B) creating FETs with gate electrodes electrically connected to  $p^{++}$ -Si; (C) coating the electronic system with PI, bonding to a temporary glass substrate, and removing the Si handle wafer by dry etching; (D) flipping the device and forming a via opening through t-SiO<sub>2</sub> to expose  $p^{++}$ -Si; (E) depositing a pH sensitive layer on top of  $p^{++}$ -Si; (F) peeling off the device from the temporary handling glass to yield a flexible electronic system.

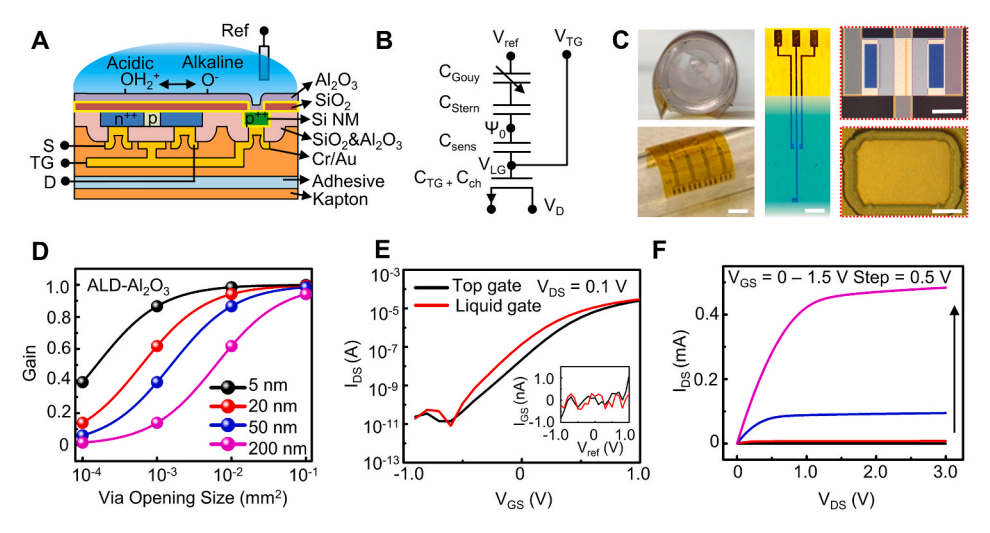


Fig. 2. Structure and electrical properties of the waterproof MOSFET. (A) Cross-section schematic illustration of a flexible electronic system highlighting the monolithic encapsulation and key functional layers. (B) Circuit diagram of the pH sensor during operation in solution. (C) Representative photographs (left and middle) and optical images (right) of such devices. The blue square overlaid on the photograph in the middle shows the part that can stay in water. The scale bars (top to bottom, left to right) are 4 mm, 1.5 mm, 200  $\mu$ m, and 30  $\mu$ m, respectively. (D) Theoretical gain value of a device with ALD-Al<sub>2</sub>O<sub>3</sub> sensing layer as a function of via opening size. (E) Transfer characteristics of a device measured by biasing the gate metal (top gate) and biasing the solution (liquid gate), respectively, and the corresponding leakage current (inset). (F) Output characteristics of a representative device. (For interpretation of the references to colour in this figure legend, the reader is referred to the Web version of this article.)

1). To avoid voltage division and signal attenuation, the gain (the ratio of  $\Delta$   $V_{th}$  to  $\Delta$   $\psi_0$ ) of the chemical sensor should be sufficiently large by properly designing the thickness of the sensing layer and the via opening size (**Supplementary Note 2**). Fig. 2D and S4 display the theoretical gain value as a function of the via opening size in devices with Al<sub>2</sub>O<sub>3</sub> and HfO<sub>2</sub> sensing interfaces, which are commonly used metal oxides for pH sensing (Rollo et al., 2020). Fig. 2E shows transfer curves of a transistor measured with  $V_{TG}$  and  $V_{LG}$ , respectively. The transistor shows a peak transconductance ( $g_m$ ) of  $5.05 \times 10^{-5}$  A V<sup>-1</sup> (Fig. S5), an on/off ratio of  $\sim 10^7$ , and a threshold voltage of  $\sim 0.4$  V. The leakage current obtained with  $V_{LG}$  is below 1 nA with no significant difference from the value recorded in the dry state (Fig. 2E, inset). Fig. 2F presents the output characteristics showing Ohmic contacts between the semiconductor and metals

Mechanical bending tests validate the flexibility of the encapsulated sensing platform. Fig. 3A shows the transfer characteristics of a test transistor before and after 400–1200 bending cycles with a bending radius of 8 mm. Fig. 3B displays the statistics regarding  $V_{th}$  of the MOSFET as a function of the bending cycle. The system maintains a stable electrical performance throughout the process with no obvious functional damages, suggesting a high mechanical stability and reliability. The excellent flexibility expands the application scenarios of such electronic devices, for example, as implantable biosensors with a minimal invasiveness needed to successfully interrogate dynamic, soft bio tissues.

#### 3.2. Stability and drift behavior of the devices in liquid environment

Systematic studies highlight the exceptional properties of the

monolithic Si and SiO2 structure as the encapsulation for biochemical sensors. While lightly doped Si show relatively high dissolution rates ranging from 20 to 70 nm  $d^{-1}$  (37 °C, pH: 7.4–7.6) (Lee et al., 2017b; Li et al., 2019; Seidel et al., 1990), dopants can modify the band edge alignment at the interface between solution and Si, and thus can affect the hydrolysis rate of Si (Si +  $4H_2O \rightarrow Si(OH)_4 + 2H_2$ ) in a tunable manner: the addition of holes in the semiconductor through p-type doping shifts the Fermi level towards the valence band. Accordingly, the width of the space-charge layer on the silicon surface decreases, which promotes electrons infused into the conduction band during chemical oxidation (Si + 4 OH $^ \rightarrow$  Si(OH)<sub>4</sub> + 4e $^-$ ) to recombine with holes in the valence band. This change at the solution-Si interface slows down the reduction of water  $(4H_2O + 4e^- \rightarrow 4OH^- + 2H_2)$ , and thus decreases the hydrolysis rate of Si (Fig. 4A). (Seidel et al., 1990) Fig. 4B and C shows the dissolution rate of key functional layers in the encapsulation stack, including Si, SiO<sub>2</sub>, and Al<sub>2</sub>O<sub>3</sub>, in PBS solution (pH = 7.4) at 37  $^{\circ}$ C. For p<sup>++</sup>-Si, the thickness decreases in a spatially uniform manner at a rate of  $\sim$ 0.20 nm d $^{-1}$ . Experiments on SiO $_2$  show a lower dissolution rate of  $\sim\!\!0.025~\text{nm}~\text{d}^{-1}$  due to the higher activation energy of  $\text{SiO}_2$  (Fang et al., 2016; Lee et al., 2017a), In contrast, Al<sub>2</sub>O<sub>3</sub> shows a negligible change in thickness within the same time scale due to its insolubility in aqueous solution. However, Al<sub>2</sub>O<sub>3</sub> gradually peels off from Si surfaces during the immersion test due to the less stable interface formed at low temperature (150 °C), leading to a nonuniformity of the surface.

Accelerated tests under elevated temperatures characterize the encapsulation capability of  $t\text{-}SiO_2$  by measuring the leakage current across the interface as a function of time. As shown in Fig. 4D, a system with a layer of  $\sim 320$  nm  $t\text{-}SiO_2$  initially shows a constant leakage current below 1 nA. During immersion in PBS, a sudden increase in the

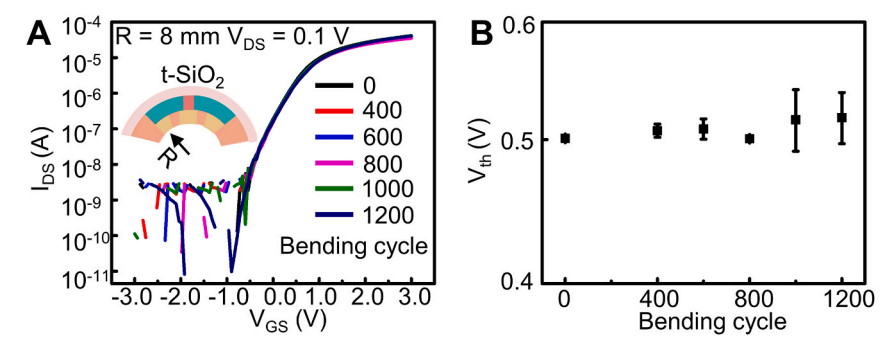


Fig. 3. Performance of the flexible, waterproof FET during bending tests. (A) Transfer characteristics of a test transistor before and after 400–1200 bending cycles (bending radius = 8 mm). (B) Threshold voltage of the transistor during bending tests.

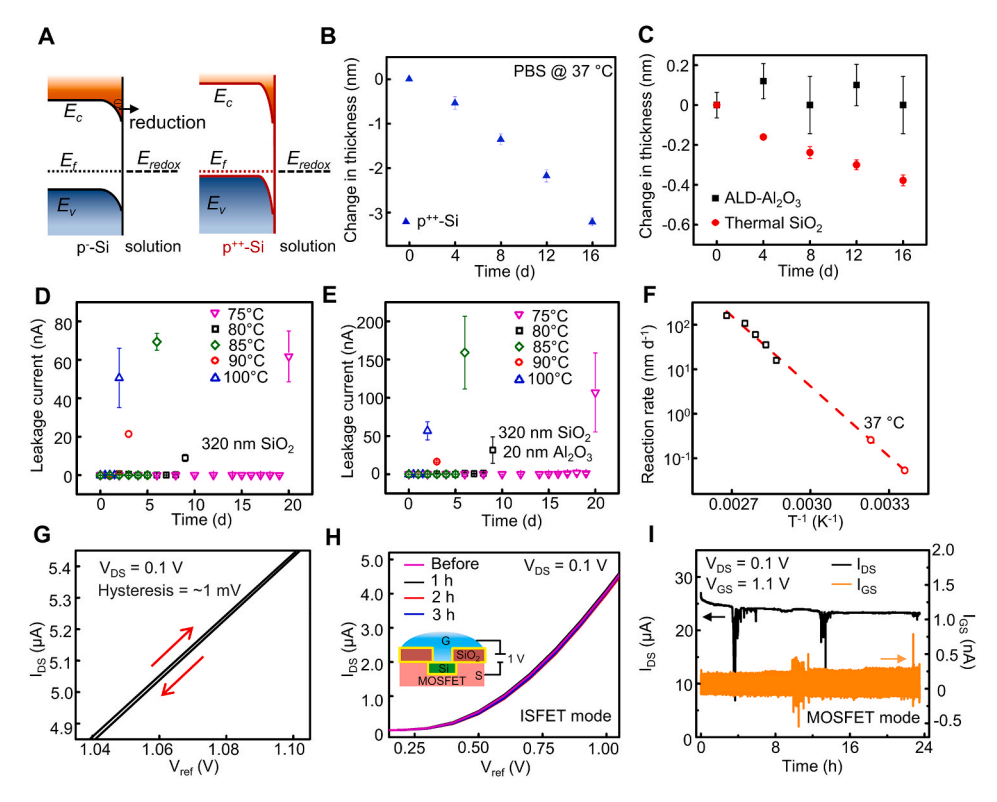


Fig. 4. Stability and drift behavior of the electronic device in liquid environment. (A) Schematic illustration of energy band diagrams of the interface between solution and p-Si with different doping concentrations. (B, C) Change in thickness of p++-Si, t-SiO2, and ALD-Al2O3 as a function of immersion time in PBS. (D, E) Leakage test results for system encapsulated with ~320 nm SiO<sub>2</sub> without (D) and with (E) a coating layer of 20 nm Al<sub>2</sub>O<sub>3</sub>. (F) Extrapolation based on leakage test results according to the Arrhenius equation. (G) Transfer curves of a device measured in a dual-sweep mode with a liquid gate. (H) Transfer curves of a device operated in ISFET mode taken between intervals of static bias applied through a liquid gate ( $V_{GS} = 1 \text{ V}$ ) for 1, 2 and 3 h. (I)  $I_{DS}$  and  $I_{GS}$  of a test device operated in MOSFET mode in PBS solution over a period of 24 h.

leakage current corresponds to the failure of the encapsulation layer which results in the penetration of liquids to the other side of the NM. The encapsulation shows a lifetime of  $\sim\!20,\,9,\,6,\,3,\,$  and 2 days at 75, 80, 85, 90 and 100 °C, respectively. Systems encapsulated with a double layer of 20 nm  $Al_2O_3$  (top) and 320 nm t-SiO\_2 (bottom) show almost the same lifespan (Fig. 4E), suggesting that the t-SiO\_2 plays a dominant role in the encapsulation quality despite the  $Al_2O_3$  of coating on top. Fitting the results according to the Arrhenius equation yields a reaction rate of  $\sim\!0.05$  nm d $^{-1}$  at 25 °C and  $\sim\!0.26$  nm d $^{-1}$  at 37 °C (Fig. 4F, Supplementary Note 3). The results suggest that the ultrathin, monocrystalline Si derived nanomembrane can provide an excellent encapsulation capability for flexible biosensors.

The signal drift behavior of the chemical sensor in the presence of a continuous bias stress is also of interest. Fig. 4G shows a zoom in view of transfer curves of a representative device fully immersed in PBS solution measured with a liquid gate in a dual sweep mode (full image in Fig. S6). The curves show an almost negligible hysteresis ( $\sim$ 1 mV), indicative of a minimum number of trapped charges in the capacitive pathway. The linearity is attributed to the mathematical relationship between  $I_{DS}$  and  $V_{GS}$  according to the following equation for a transistor operating in the triode region (0 <  $V_{DS}$  <  $V_{GS}$  -  $V_{th}$ ) (Sze et al., 2021):

$$I_{DS} = \mu C_{ox} \frac{w}{L} \left( V_{GS} - V_{th} - \frac{V_{DS}}{2} \right) V_{DS}$$
 (2)

where  $\mu$  is the mobility of the charge carriers,  $C_{ox}$  is the capacitance of the dielectric layer(s), W and L are the width and length of the channel, respectively. The advantage of the linearity is that the value of  $g_m$  is a constant which allows for the accurate prediction of pH changes despite the shift of the transfer curves. A higher slope value is desirable for achieving a larger signal output upon the same change in surface potential. This can be achieved by increasing W or decreasing L according to Equation (2). A set of transfer curves of the device scanned between intervals of a bias applied through the liquid gate appears in Fig. 4H (i.e., operation in ISFET mode). The key performance characteristics of the transistor remains constant upon the application of a static bias of 1 V. The liquid gate bias can serve as a driving force that impels the transport

of ions through the encapsulation layer. (Song et al., 2019) The results here suggest that the encapsulation effectively retards the permeation of charged species into the active electronic components under the current experimental settings.

The study also investigates the impact of the gate voltage applied through the terminal pad (i.e., operation in MOSFET mode). Fig. 4I shows  $I_{DS}$  and  $I_{GS}$  of a transistor operated in PBS under a fixed bias condition ( $V_{GS} = 1.1 \text{ V}$ ,  $V_{DS} = 0.1 \text{ V}$ ) over a period of 24 h.  $I_{GS}$  remains well below 1 nA throughout the whole process (the occasional deviations from the baselines may be associated with noises from the environment). After the initial stabilization with a relatively abrupt drift ( $\sim$ 34 mV during the first hour),  $I_{DS}$  shows a slow drift that corresponds to an increase in  $V_{th}$  of ~35 mV (i.e., ~1.5 mV h<sup>-1</sup>). Since there is no liquid gate bias applied across the encapsulation, the value here may represent the drift associated with intrinsic factors of the device (Jamasb et al., 1998). The transfer curves before and after the application of the static bias appear in Fig. S7, showing a permanent increase in  $V_{th}$  of  $\sim 30$ mV, in contrast to the total value of  $\sim$ 70 mV calculated using  $I_{DS}$  drift in Fig. 4I. The results indicate that the drift during the operation in MOS-FET mode originates from more than one reason: the initial current settling is associated with changes in trap state occupancy induced by the gate bias, and electrical grounding such as gate voltage sweep can reverse this process by redistributing charges in these trap states (Noyce et al., 2019). The permanent, slower drift resulting in  $V_{th}$  increase, is likely due to irreversible changes caused by the sustained electrical bias, such as the migration of charged impurities trapped in the gate oxide of the transistor. Experiment with a higher bias stress ( $V_{GS} = 2.5 \text{ V}$ ) shows qualitatively similar results with an abrupt initial drift followed by a slow drift (Fig. S8). For long-term applications, it is necessary to consider both drift modes (i.e., ISFET vs. MOSFET mode) for signal calibration to ensure a high sensing accuracy.

# 3.3. Characterization of pH sensing performance

Electrical characterization evaluates the response of the transistors with an  $Al_2O_3$  sensing layer functionalized on the Si gate electrode to

standard pH buffer solutions. Fig. 5A shows the transfer characteristics in linear scale in buffer solutions with pH values ranging from 4.0 to 9.0. Driven by the chemical equilibrium, an increased pH causes deprotonation of the hydroxyl groups on Al<sub>2</sub>O<sub>3</sub>. The change in surface potential due to an increased number of negative charges results in a shift in  $V_{th}$ towards the positive direction according to Equation (1). Corresponding transfer curves in log scale appear in Fig. S9. Fig. 5B shows extracted  $V_{th}$  as a function of pH value, suggesting a sensitivity of 58.5  $\pm$  3.9 mV pH<sup>-1</sup>. The theoretical maximum sensitivity can be calculated using the Nernst equation (i.e., the "Nernst limit") (Supplementary Note 4) (Kaisti, 2017). The result suggests a superior property of the sensor design that combines Al<sub>2</sub>O<sub>3</sub> as the pH sensitive interface and Si FET as the backplane signal transducer. Statistics of the sensitivity of seven different devices demonstrate only minor device-to-device variation (Fig. 5C), with an average of 53.0 mV pH<sup>-1</sup> and a medium of 52.8 mV pH $^{-1}$ . Similarly, measuring  $I_{DS}$  as a function of time shows responses to pH variations (Fig. 5D). The step of the height is close to the Nernst Limit, consistent with results extracted from the transfer curves. In contrast, a device with bare Si (i.e., without metal oxide coating) yields a sensitivity of 32.8  $\pm$  2.9 mV pH<sup>-1</sup>, which is likely due to the response of native SiO<sub>2</sub> on Si (Fig. S10).

Fig. 5E and F shows transfer curves and extracted  $V_{th}$  of a transistor with Al<sub>2</sub>O<sub>3</sub> in response to NaCl solution (concentration: from 60 to 100 mM). The transfer curves show a negative shift upon the increase in NaCl concentration with a sensitivity of  $-47.3 \pm 1.1$  mV dec<sup>-1</sup>, suggesting that the interface layer mainly interacts with cations instead of anions in the test environment. The observation can be explained by previous studies that hydroxyl groups on metal oxide can also respond to other ions in addition to protons (Wang et al., 2019). However, it should be noted that results here are different from an earlier report that metal oxide surface interacts with anions (Tarasov et al., 2012). The reason could be associated with the fact that multiple factors, such as the pH and ionic strength of the test solutions, may affect the surface states of metal oxide and determine the interaction mode with ions. Integration of ion-selective membranes on the gate electrode of the potentiometric sensors will allow for the capture and detection of ions with a high selectivity (Lahav et al., 2001; Lee and Cui, 2010; Mu et al., 2014; Schuett et al., 2016; Zayats et al., 2006).

# 3.4. Application of the pH sensors in monitoring external biochemical processes

The pH sensors are capable of real-time monitoring of biochemical reactions by quantifying minute changes in pH due to proton release/uptake during enzymatic catalysis (Fig. 6A). Urea is a biomarker that can

be found in a variety of biofluids including blood, sweat and urine. The concentration of urea can be used in diagnostic measure of renal, heart and/or liver diseases (Huang et al., 2002; Keller et al., 2016). The hydrolysis of one urea molecule releases two ammonia and one carbon dioxide which then form ammonium and bicarbonate in solution, respectively. The net increase in OH concentration results in a sequential increase in pH. Fig. 6B shows the real-time response of a pH sensor to this reaction using urea solutions with varied concentrations (from 0.5 to 40 mM in PBS solution) and 1 mL urease solution (Canavalia ensiformis; concentration: 90 U mL-1) pipetted into the system. The decrease in  $I_{DS}$  during the reaction indicates an increased number of negative charges at the sensing interface. The signal amplitude positively relates to the original concentration of urea. Measured changes in pH using the FET sensor and a commercial pH meter appear in Fig. 6C (Supplementary Note 5). The pH sensing platform allows for the investigation of enzyme kinetics. Fig. 6D shows the extracted changing speed of H<sup>+</sup> and OH<sup>-</sup> (absolute value) during the initial states of these reactions (0-100 s). With a fixed amount of urease and an increasing concentration of urea, both the changing rates of H<sup>+</sup> and OH<sup>-</sup> gradually increase. As these two values are positively related to the reaction speed, the results presented here are qualitatively consistent with the model described by the Michaelis-Menten equation (Kim et al., 2020).

The use of the pH sensor also allows for the study on enzyme activity. An example using penicillin and penicillinase appears in Fig. 6E (Davies and Davies (2010); Lobanovska and Pilla, 2017). The hydrolysis of a penicillin G molecule yields a penicilloic acid which releases an extra proton. The concentration of penicillinase from Bacillus cereus (EC 3.5.2.6; Sigma Aldrich) used in this study ranges from  $0.2 \text{ U mL}^{-1}$  to 200U mL<sup>-1</sup>.1 mL penicillinase solution is added into 20 mL penicillin G solution with a concentration of 30 mM, the value of which is much higher than the  $K_m$  of penicillinase (60  $\mu M$ ) (Heckler and Day, 1983; Myers and Shaw, 1989) to ensure that all systems show a zero-order kinetics behavior with the reaction rate approaching the maximum value. Recording of  $I_{DS}$  after the injection of penicillinase solutions shows a general trend of increase corresponding to a decrease in pH (Fig. 6E). Fig. 6F shows the comparison between calculated pH values and those obtained using a commercial pH meter. By assuming that the changing speed of H<sup>+</sup> concentration in this reaction is proportional to the consumption rate of the substrate, the initial reaction rate (i.e., the maximum reaction rate with the corresponding enzyme concentration) represented by this value demonstrates a linear relationship with the concentration of penicillinase (Fig. 6G). The slope of the curve corresponds to the maximum amount of proton produced per unit concentration of penicillinase per second.

Finally, this sensing platform can detect cumulative changes in pH

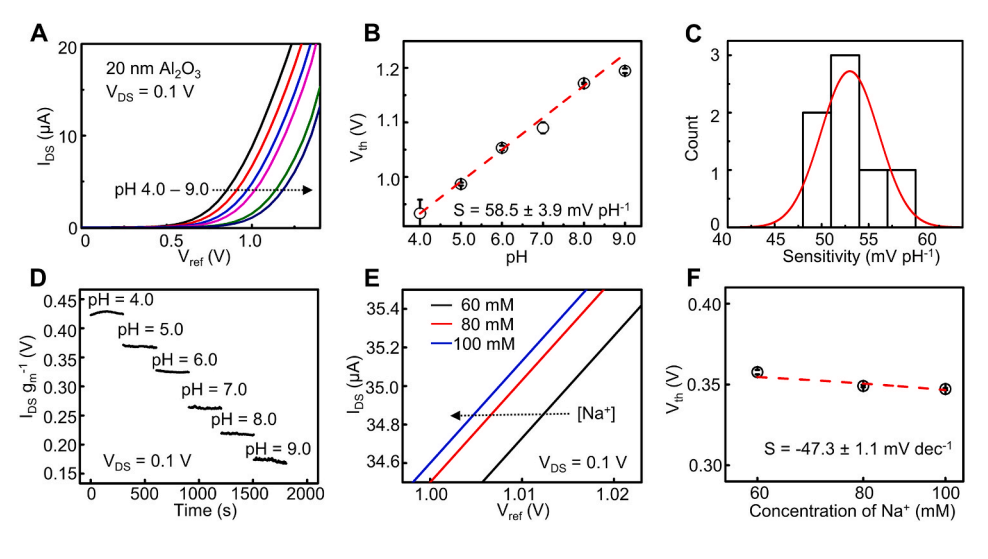


Fig. 5. Evaluation of pH sensing performance of the electronic device. (A) Linear scale transfer characteristics of a pH sensor with 20 nm  ${\rm Al_2O_3}$  in response to buffer solutions with pH values ranging from 4.0 to 9.0. (B) pH sensitivity of the representative device in Fig. 5A. (C) Histogram of sensitivity measured from 7 different devices with an  ${\rm Al_2O_3}$  sensing layer. (D) pH measurement results as a function of time. (E) Transfer curves of a test device in response to solutions with different concentrations of Na $^+$  (60–100 mM). (F) Extracted threshold voltage of the device in Fig. 5E.

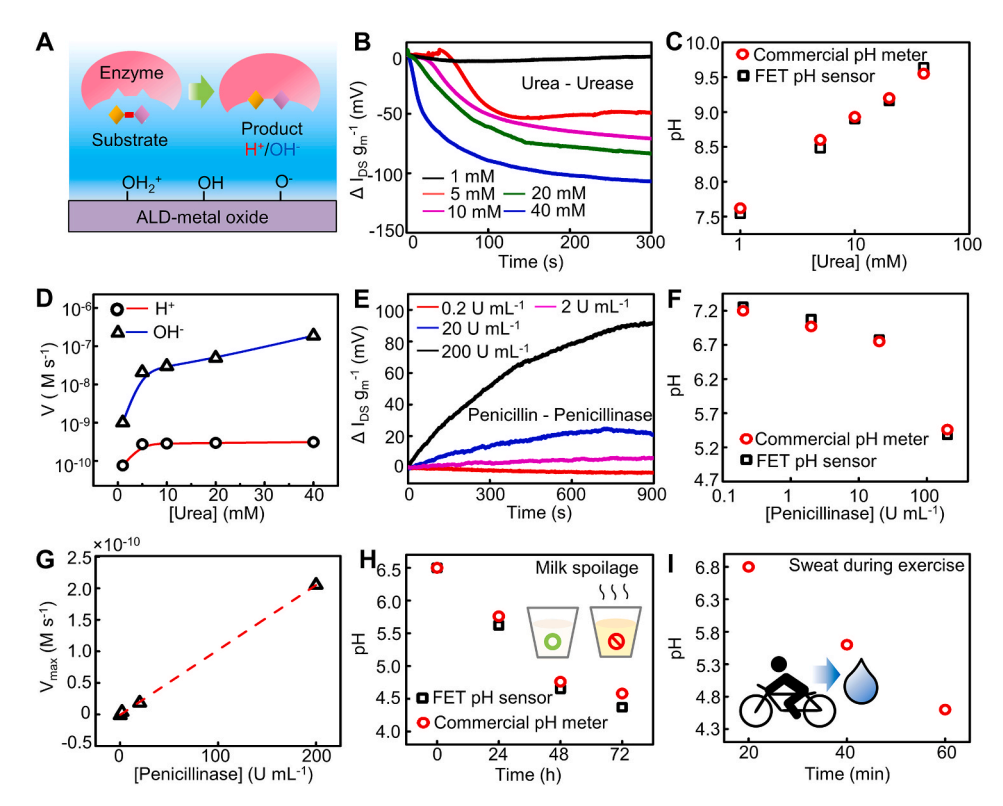


Fig. 6. (A) Schematic illustration showing monitoring of biochemical reactions via an "enzymatic amplification" effect. (B) Current signals (normalized according to  $g_m$ ) of the urea-urease reaction with the substrate concentration ranging from 1 to 40 mM. (C) Extracted changes in pH value based on results in Fig. 6B, and results measured using a commercial pH meter. (D) The changing speed of [H+] and [OH<sup>-</sup>] during the initial stage of the reaction as a function of urea concentration. (E) Current signals (normalized according to  $g_m$ ) of the penicillin-penicillinase reaction with the enzyme concentration ranging from 0.2 to 200 U mL<sup>-1</sup>. (F) Extracted changes in pH value based on results in Fig. 6E, and results measured using a commercial pH meter. (G) Maximum reaction rates represented by the changing speed of [H<sup>+</sup>] as a function of penicillinase concentration. (H) Results of the milk spoilage test. (I) Results of sweat pH monitoring during a 60 min exercise

value in complex system caused by multiple chemical reactions relevant to food quality and health status monitoring. Fig. 6H and S11A show the change in pH value of a cup of milk during a 72-h spoilage process at room temperature (25 °C). Spoilage happens at a storage temperature high enough for the growth of fermentative bacteria. The fermentation produces multiple acids, such as acetic and propionic acids (Erkmen and Bozoglu, 2016). The result shows a decrease in pH value of approximately 0.9 after 24 h, 1.8 after 48 h, and 2.1 after 72 h, respectively. Minor discrepancies with values obtained using the commercial pH meter could be associated with non-specific interactions discussed in the preceding section. Similarly, the sensor can monitor sweat pH representing changes in physiological processes. Fig. 6I, S11B and S11C show examples of sweat pH tracking during exercise where the sweat becomes more acidic over time. The observation here could be associated with the following reasons: during exercise, the body metabolism becomes more active, resulting in the production of an increased amount of CO2 and H+ due to enhanced respiration. Moreover, an anaerobic metabolism occurs when the lung can not supply enough O2 as demanded by the muscle for energy. The production of adenosine triphosphate through energy pathways in the absence of O2 yields lactic acid. These physiological processes lead to an increased acidity in sweat (Coyle et al., 2010).

# 4. Conclusions

In summary, the results presented in this study describe a materials strategy and integration scheme that exploit submicron Si derived NMs as a waterproof encapsulation for potentiometric biochemical sensors. Systematic studies reveal that this ultrathin, yet dense and stable structure enables high-fidelity and continuous operation of transistors in biofluids under bias stress with a minimum level of hysteresis ( $\sim 1$  mV) and leakage current (< 1 nA). The coupling between the backplane transistors and functional layers provides the electronic devices with a capability of potentiometric sensing. Studies on signal drfit behavior in solution suggest that two drift modes (ISFET vs. MOSFET) should be considered, and the drift contains a reversible and an irreversible part. The study demonstrates a sensing platform with a near-Nernstian

sensitivity for pH sensing with metal oxide as the sensing layer. Demonstrations of multiple applications suggest the broad applicability of this platform in analytical chemistry, food quality monitoring, and healthcare. In addition to the potentiometric sensing described in this work, designing other types of waterproof Si electronics (e.g., Si optical sensors) is also possible by following this integration scheme using CMOS technologies (Xu, 2021). Although the current work focuses on sensor development and pH sensing, such a device can potentially find applications in monitoring bio-related processes via the integration of bio-recognition elements (e.g., antibodies, aptamers, enzymes, and molecularly imprinted polymers). Examples include but are not limited to biomedical devices with biocompatibility, bioconformality, and biostability for applications in closed-loop neuromodulation and neuroscience research. Furthermore, beyond the sensing capability, integrating bio-components on the side of the waterproof electronic systems in contact with biofluids can enable interactions with the biological system. Immediate opportunities are development of flexible and waterproof CMOS-based chemical sensor arrays with active functionalities for real-time imaging of biomarker concentration and flow with a high spatiotemperoal resolution.

#### CRediT authorship contribution statement

Shulin Chen: Conceptualization, Methodology, Writing – original draft, Preparation, Review & Editing, Writing – review & editing. Yan Dong: Methodology, Writing – review & editing. Tzu-Li Liu: Methodology, Writing – review & editing. Jinghua Li: Conceptualization, Methodology, Writing – original draft, Preparation, Review & Editing, Writing – review & editing, Supervision.

### Declaration of competing interest

The authors declare that they have no known competing financial interests or personal relationships that could have appeared to influence the work reported in this paper.

#### Acknowledgements

This work was support by The The Ohio State University start-up funds, the Chronic Brain Injury Pilot Award Program, and the National Center For Advancing Translational Sciences (Award Number: UL1TR002733). The content is solely the responsibility of the authors and does not necessarily represent the official views of the National Center For Advancing Translational Sciences or the National Institutes of Health. This work was also supported in part by The Ohio State University Materials Research Seed Grant Program, funded by the Center for Emergent Materials, an NSF-MRSEC, grant DMR-2011876, the Center for Exploration of Novel Complex Materials, the Institute for Materials Research. S. C. acknowledges the University Fellowship from the graduate school at The Ohio State University.

#### Appendix A. Supplementary data

Supplementary data to this article can be found online at https://doi.org/10.1016/j.bios.2021.113683.

#### References

- Agoston, D.V., Shutes-David, A., Peskind, E.R., 31(9)(2017), pp. 1195-1203.
- Andreu-Perez, J., Leff, D.R., Ip, H.M., Yang, G.Z., 2015. IEEE Trans. Biomed. Eng. 62 (12), 2750–2762.
- Arakawa, T., Kuroki, Y., Nitta, H., Chouhan, P., Toma, K., Sawada, S., Takeuchi, S., Sekita, T., Akiyoshi, K., Minakuchi, S., Mitsubayashi, K., 2016. Biosens. Bioelectron. 84, 106–111.
- Arvand, M., Ghodsi, N., 2014. Sensor. Actuator. B Chem. 204, 393-401.
- Asher, S.A., Peteu, S.F., Reese, C.E., Lin, M., Finegold, D., 2002. Anal. Bioanal. Chem. 373 (7), 632–638.
- Ausländer, D., Ausländer, S., Charpin-El Hamri, G., Sedlmayer, F., Müller, M., Frey, O., Hierlemann, A., Stelling, J., Fussenegger, M., 2014. Mol. Cell. 55 (3), 397–408.
- Bae, T.E., Jang, H.J., Yang, J.H., Cho, W.J., 2013. ACS Appl. Mater. Interfaces 5 (11), 5214–5218.
- Chen, K.-I., Li, B.-R., Chen, Y.-T., 2011. Nano Today 6 (2), 131–154.
- Coyle, S., Lau, K.T., Moyna, N., O'Gorman, D., Diamond, D., Di Francesco, F., Costanzo, D., Salvo, P., Trivella, M.G., De Rossi, D.E., Taccini, N., Paradiso, R., Porchet, J.A., Ridolfi, A., Luprano, J., Chuzel, C., Lanier, T., Revol-Cavalier, F., Schoumacker, S., Mourier, V., Chartier, I., Convert, R., De-Moncuit, H., Bini, C., 2010. IEEE Trans. Inf. Technol. Biomed. 14 (2), 364–370.
- Davies, J., Davies, D., 2010. Mol. Biol. Rev. 74 (3), 417-433.
- Elyasi, A., Fouladian, M., Jamasb, S., 2018. IEEE J. Electron Devices Soc. 6, 747–754.
  Erkmen, O., Bozoglu, T.F., 2016. Food Microbiology, 2 Volume Set: Principles into Practice. John Wiley & Sons.
- Fang, H., Zhao, J., Yu, K.J., Song, E., Farimani, A.B., Chiang, C.H., Jin, X., Xue, Y., Xu, D., Du, W., Seo, K.J., Zhong, Y., Yang, Z., Won, S.M., Fang, G., Choi, S.W., Chaudhuri, S., Huang, Y., Alam, M.A., Viventi, J., Aluru, N.R., Rogers, J.A., 2016. Proc. Natl. Acad. Sci. U.S.A. 113 (42), 11682–11687.
- Gao, W., Emaminejad, S., Nyein, H.Y.Y., Challa, S., Chen, K., Peck, A., Fahad, H.M., Ota, H., Shiraki, H., Kiriya, D., Lien, D.H., Brooks, G.A., Davis, R.W., Javey, A., 2016. Nature 529 (7587), 509–514.
- Garcia-Cordero, E., Bellando, F., Zhang, J., Wildhaber, F., Longo, J., Guérin, H., Ionescu, A.M., 2018. ACS Nano 12 (12), 12646–12656.
- Heckler, T.G., Day, R.A., 1983. Biophys. Acta 745 (3), 292-300.
- Huang, C.T., Chen, M.L., Huang, L.L., Mao, I.F., 2002. Chin. J. Physiol. 45 (3), 109–115. Iguchi, S., Kudo, H., Saito, T., Ogawa, M., Saito, H., Otsuka, K., Funakubo, A.,
- Mitsubayashi, K., 2007. Biomed. Microdevices 9 (4), 603–609. Jamasb, S., Collins, S., Smith, R.L., 1998. Sensor. Actuator. B Chem. 49 (1–2), 146–155. Janata, J., 1994. Analyst 119 (11), 2275–2278.
- Kaisti, M., 2017. Biosens. Bioelectron. 98, 437–448.
- Keller, R.W., Bailey, J.L., Wang, Y., Klein, J.D., Sands, J.M., 2016. Phys. Rep. 4 (11), e12825.
- Kim, J., Kim, M., Lee, M.S., Kim, K., Ji, S., Kim, Y.T., Park, J., Na, K., Bae, K.H., Kyun
  Kim, H., Bien, F., Young Lee, C., Park, J.U., 2017. Nat. Commun. 8, 14997.
  Kim, J., Campbell, A.S., Wang, J., 2018a. Talanta 177, 163–170.

- Kim, S., Kwon, D.W., Kim, S., Lee, R., Kim, T.H., Mo, H.S., Kim, D.H., Park, B.G., 2018b. Curr. Appl. Phys. 18, S68–S74.
- Kim, S.B., Koo, J., Yoon, J., Hourlier-Fargette, A., Lee, B., Chen, S., Jo, S., Choi, J., Oh, Y. S., Lee, G., Won, S.M., Aranyosi, A.J., Lee, S.P., Model, J.B., Braun, P.V., Ghaffari, R., Park, C., Rogers, J.A., 2020. Lab Chip 20 (1), 84–92.
- Koh, A., Kang, D., Xue, Y., Lee, S., Pielak, R.M., Kim, J., Hwang, T., Min, S., Banks, A., Bastien, P., Manco, M.C., Wang, L., Ammann, K.R., Jang, K.I., Won, P., Han, S., Ghaffari, R., Paik, U., Slepian, M.J., Balooch, G., Huang, Y., Rogers, J.A., 2016. Sci. Transl. Med. 8 (366), 366ra165.
- Lahav, M., Kharitonov, A.B., Katz, O., Kunitake, T., Willner, I., 2001. Anal. Chem. 73 (3), 720–723.
- Lanuzza, M., Strangio, S., Crupi, F., Palestri, P., Esseni, D., 2015. IEEE Trans. Electron. Dev. 62 (12), 3973–3979.
- Lee, D., Cui, T., 2010. Biosens. Bioelectron. 25 (10), 2259-2264.
- Lee, C.S., Kim, S.K., Kim, M., 2009. Sensors 9 (9), 7111-7131.
- Lee, Y.K., Yu, K.J., Kim, Y., Yoon, Y., Xie, Z., Song, E., Luan, H., Feng, X., Huang, Y., Rogers, J.A., 2017a. ACS Appl. Mater. Interfaces 9 (49), 42633–42638.
- Lee, Y.K., Yu, K.J., Song, E., Barati Farimani, A., Vitale, F., Xie, Z., Yoon, Y., Kim, Y., Richardson, A., Luan, H., Wu, Y., Xie, X., Lucas, T.H., Crawford, K., Mei, Y., Feng, X., Huang, Y., Litt, B., Aluru, N.R., Yin, L., Rogers, J.A., 2017b. ACS Nano 11 (12), 12562–12572.
- Lee, H., Hong, Y.J., Baik, S., Hyeon, T., Kim, D.H., 2018. Adv. Healthc. Mater. 7 (8), e1701150.
- Levey, A.S., Coresh, J., 2012. Lancet 379 (9811), 165-180.
- Li, J., Li, R., Chiang, C.H., Zhong, Y., Shen, H., Song, E., Hill, M., Won, S.M., Yu, K.J., Baek, J.M., Lee, Y., Viventi, J., Huang, Y., Rogers, J.A., 2019. Adv. Mater. Technol. 5 (1), 1900800.
- Lobanovska, M., Pilla, G., 2017. Yale J. Biol. Med. 90 (1), 135-145.
- Lucisano, J.Y., Routh, T.L., Lin, J.T., Gough, D.A., 2017. IEEE Trans. Biomed. Eng. 64 (9), 1982–1993.
- Malon, R.S., Sadir, S., Balakrishnan, M., Córcoles, E.P., 2014. BioMed Res. Int. 962903, 2014.
- Mao, S., Chang, J., Pu, H., Lu, G., He, Q., Zhang, H., Chen, J., 2017. Chem. Soc. Rev. 46 (22), 6872–6904.
- Martín, A., Kim, J., Kurniawan, J.F., Sempionatto, J.R., Moreto, J.R., Tang, G., Campbell, A.S., Shin, A., Lee, M.Y., Liu, X., Wang, J., 2017. ACS Sens. 2 (12), 1860–1868.
- Mu, L., Droujinine, I.A., Rajan, N.K., Sawtelle, S.D., Reed, M.A., 2014. Nano Lett. 14 (9), 5315–5322.
- Myers, J.L., Shaw, R.W., 1989. Biochim. Biophys. Acta 995 (3), 264-272.
- Nguyen, L.D., Larson, L.E., Mishra, U.K., 1992. Proc. IEEE 80 (4), 494–518.
- Noyce, S.G., Doherty, J.L., Cheng, Z., Han, H., Bowen, S., Franklin, A.D., 2019. Nano Lett. 19 (3), 1460–1466.
- Pandya, D., Nagrajappa, A.K., Ravi, K.S., 2016. J. Clin. Diagn. Res. 10 (10), ZC58–ZC62.Pavuluri, K., Manoli, I., Pass, A., Li, Y., Vernon, H.J., Venditti, C.P., McMahon, M.T., 2019. Sci Adv 5 (8), eaaw8357.
- Renda, R., 2017. Ren. Fail. 39 (1), 452-457.
- Rollo, S., Rani, D., Olthuis, W., García, C.P., 2020. Sensor. Actuator. B Chem. 303, 127215
- Rose, D.P., Ratterman, M.E., Griffin, D.K., Hou, L., Kelley-Loughnane, N., Naik, R.R., Hagen, J.A., Papautsky, I., Heikenfeld, J.C., 2015. IEEE Trans. Biomed. Eng. 62 (6), 1457–1465.
- Schuett, J., Ibarlucea, B., Illing, R., Zoergiebel, F., Pregl, S., Nozaki, D., Weber, W.M., Mikolajick, T., Baraban, L., Cuniberti, G., 2016. Nano Lett. 16 (8), 4991–5000.
- Seidel, H., Csepregi, L., Heuberger, A., Baumgärtel, H., 1990. J. Electrochem. Soc. 137 (11), 3626–3632.
- Song, E., Li, J., Rogers, J.A., 2019. Apl. Mater. 7 (5), 050902.
- Sze, S.M., Li, Y., Ng, K.K., 2021. Physics of Semiconductor Devices, fourth ed. John Wiley & Sons.
- Tarasov, A., Wipf, M., Stoop, R.L., Bedner, K., Fu, W., Guzenko, V.A., Knopfmacher, O., Calame, M., Schönenberger, C., 2012. ACS Nano 6 (10), 9291–9298.
- Wang, Y., Wang, S., Tao, L., Min, Q., Xiang, J., Wang, Q., Xie, J., Yue, Y., Wu, S., Li, X., Ding, H., 2015. Biosens. Bioelectron. 65, 31–38.
- Wang, R., DelloStritto, M., Remsing, R.C., Carnevale, V., Klein, M.L., Borguet, E., 2019.
  J. Phys. Chem. C 123 (25), 15618–15628.
- Wu, K., Zhang, H., Chen, Y., Luo, Q., Xu, K., 2021. IEEE Electron. Device Lett. 42 (4), 541–544.
- Xu, K., 2021. J. Micromech. Microeng. 31 (5), 054001.
- Zayats, M., Huang, Y., Gill, R., Ma, C.A., Willner, I., 2006. J. Am. Chem. Soc. 128 (42), 13666–13667.
- Zhang, Y., Guo, H., Kim, S.B., Wu, Y., Ostojich, D., Park, S.H., Wang, X., Weng, Z., Li, R., Bandodkar, A.J., Sekine, Y., Choi, J., Xu, S., Quaggin, S., Ghaffari, R., Rogers, J.A., 2019. Lab Chip 19 (9), 1545–1555.